INFLUENCE OF THE FREE-STREAM TURBULENCE ON THE ONSET OF WAVE FORMATION

Romain Mathis
Institut de Mécanique des Fluides de Toulouse
Université de Toulouse, CNRS, INPT, UPS
Toulouse, France
romain.mathis@imft.fr

Sébastien Cazin
Institut de Mécanique des Fluides de Toulouse
Université de Toulouse, CNRS, INPT, UPS
Toulouse, France
sebastien.cazin@imft.fr

Jeanne Methel
Institut de Mécanique des Fluides de Toulouse
Université de Toulouse, CNRS, INPT, UPS
Toulouse, France
jeanne.methel@imft.fr

François Charru
Institut de Mécanique des Fluides de Toulouse
Université de Toulouse, CNRS, INPT, UPS
Toulouse, France
francois.charru@imft.fr

Jacques Magnaudet
Institut de Mécanique des Fluides de Toulouse
Université de Toulouse, CNRS, INPT, UPS
Toulouse, France
jacques.magnaudet@imft.fr

Frédéric Moisy
Université Paris-Saclay, CNRS, FAST
F-91405, Orsay, France
frederic.moisy@universite-paris-saclay.fr

Marc Rabaud
Université Paris-Saclay, CNRS, FAST
F-91405, Orsay, France
marc.rabaud@universite-paris-saclay.fr

Introduction

The generation of wind-driven waves is of central importance for wave forecasting and for engineering applications involving liquid–gas transport (Sullivan & McWilliams, 2010; Janssen, 2004). Since the pioneering works of Phillips (1957) and Miles (1957), decades of research have converged on a two-stage scenario. In the first stage, incoherent, low-amplitude wrinkles are excited by turbulent pressure fluctuations in the air, leading to a *linear* growth of wave energy in time (Phillips, 1957), with saturation at a finite amplitude set by liquid viscosity for moderate winds (Paquier *et al.*, 2016; Perrard *et al.*, 2019). In the second stage, at sufficiently strong winds, the air–water shear flow becomes unstable, producing an *exponential* growth of wave energy (Miles, 1957).

Yet the nature of the transition between the Phillips and Miles regimes, and its dependence on physical parameters, remains unsettled. This motivates accurate laboratory measurements under controlled conditions, especially for parameter ranges distinct from the classical air–water system.

Two factors of particular interest are liquid viscosity and free-stream turbulence intensity—parameters that are often neglected or difficult to vary in both experiments and simulations. The wide scatter in reported onset velocities for the air–water configuration may partly reflect uncontrolled variations in free-stream turbulence. While the role of viscosity on wrinkle amplitude and the wrinkle–wave transition has been examined experimentally (Paquier *et al.*, 2016), the present work focuses on the influence of free-stream turbulence.

The aim of the present study is to investigate how the onset velocity for wave amplification is affected by changing the turbulent nature of the incoming flow, in particular the turbulence level or geometrical features of the boundary layers. To this end, we designed a dedicated experiment aimed at modifying the properties of the incoming turbulence by using turbulence grids to control the level of the turbulence of the wind developing over a viscous fluid, combined with hot-wire anemometry, PIV and Free-surface synthetic Schlieren measurements (Moisy *et al.*, 2009) to characterise the air and liquid flows as well as the surface deformation.

Experimental Methods

The experiments were conducted in the closed-loop wind tunnel S2 of IMFT, which has a working test-section of dimensions $1.8\,\mathrm{m} \times 0.5\,\mathrm{m} \times 0.5\,\mathrm{m}$. The whole floor of the wind-tunnel is replaced by a tank of depth $h = 50\,\mathrm{mm}$, filled with silicon oil of density $\rho = 1.2 \times 10^3\,\mathrm{kg\,m^{-3}}$ and kinematic viscosity $\nu = 50 \times 10^{-6}\,\mathrm{m\,s^{-2}}$. This large viscosity produces a strong attenuation of the waves, avoiding wave reflections on side walls and at the extremity of the tank (Paquier *et al.*,

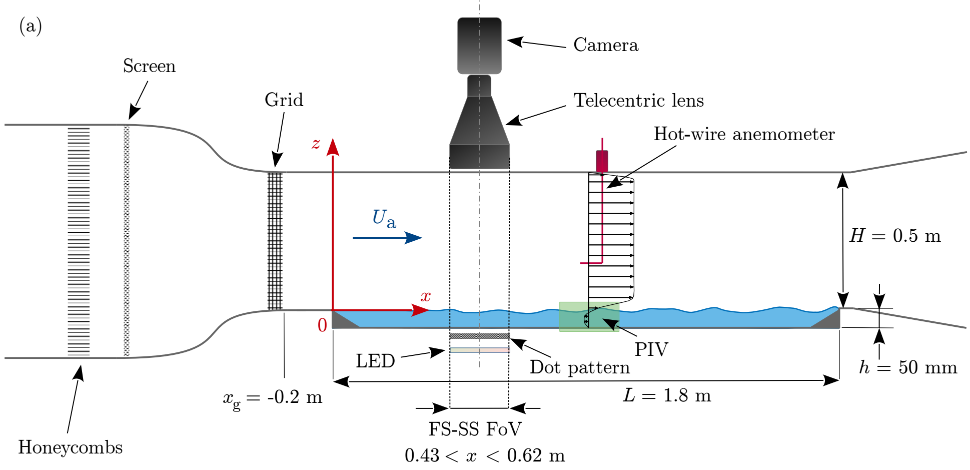

Figure 1. Experimental set-up of the wind tunnel equipped with a 50 mm depth liquid tank at the bottom. Also depicted are the three measurement techniques used.

2016). Both the wind-tunnel side walls and the liquid tank are made of glass to enable optical access.

Multiple measurement techniques were carried out in order to characterise the air and viscous fluid, as well as their interface:

1. hot-wire anemometry measurements, to characterise the free-stream turbulence intensity u'/U_a and the boundary layer profile developing over the liquid;
2. particle image velocimetry measurements in a vertical plane in the liquid to measure the surface drift velocity, from which we deduce the friction velocity u^* using the shear stress continuity at the surface;
3. surface deformation measurements using Free Surface Synthetic Schlieren (FSSS), to measure the wave growth amplitude with micrometer accuracy.

To investigate the influence of the free-stream turbulence on the wave generation, different grids have been mounted at the inlet of the test-section. Three inflow conditions are studied : the empty wind tunnel (NG), and two turbulent grids, G32 and G64, with mesh sizes $M = 31.6$ mm and 64.1 mm, respectively. The grids are made of square-mesh arrays of co-planar rectangular bars, and have the same porosity ratios $\beta = (1 - d/M)^2 = 0.66$. Such grids are expected to generate nearly isotropic turbulence, with low Reynolds number dependence (Roach, 1987). As shown in figure 2, the no-grid inflow condition produces a free-stream turbulence level $u'/U_a \simeq 0.6\%$, with no variation in the streamwise direction, while the grids G32 and G64 produce a decreasing turbulence level along the wind-tunnel, in the range $13-2\%$ and $26-4\%$, respectively. The typical levels T_u reach in the FS-SS window (the grey strip in figure 2) are $T_u \simeq 3-4\%$ (G32) and $7-9\%$ (G64). The decay of the turbulence intensity is found to follows the classical power-law behavior of grid-generated turbulence,

$$T_u = \frac{\sqrt{\overline{u'^2}}}{U_a} = a\left(\frac{X - X_0}{M}\right)^{-n}, \tag{1}$$

with X_0 a virtual origin, n the decay exponent and a a prefactor. A best-fit procedure, treating X_0 and n as free parameters, yields $X_0/M \simeq 1$ and $n \simeq 0.82 \pm 0.02$. Values of n reported in the literature typically fall within the range $0.55 < n < 0.7$, indicating that the present results lie slightly above the upper bound of this interval (Mohamed & LaRue, 1990; Lavoie *et al.*, 2007; Zhao *et al.*, 2023). This discrepancy may be partly explained by the relatively short downstream distances considered here, $X/M \simeq 2$–50, whereas significantly larger distances ($X/M > 40$) are usually examined in previous studies. Such short distances are required in the present work to maintain high turbulence intensities, thereby ensuring a significant influence of free-stream turbulence on the wave generation process.

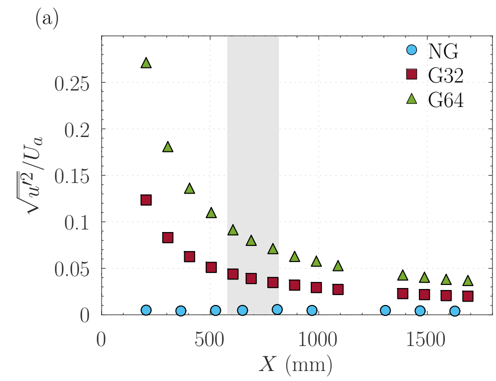

Figure 2. Streamwise evolution of T_u for $U_a = 3.2\,\mathrm{m\,s^{-1}}$ (hot wire measurements). The light grey strip marks the streamwise extent of the FS-SS measurements.

Effect on friction velocity

The formation of surface waves is directly tied to wind-induced shear stress at the air-liquid interface, defined as $\tau = \mu_a \partial\overline{u}/\partial z$. This quantity is commonly parameterised through the friction velocity, $u^* = \sqrt{\tau/\rho_a}$. A direct determination of τ is hindered by the inability of hot-wire anemometry to resolve the velocity gradient in the immediate vicinity of the interface with sufficient accuracy. Consequently, τ is typically inferred indirectly. In canonical boundary layers, where free-stream turbulence is negligible, u^* may be obtained by fitting the mean velocity profile to the logarithmic law of the wall. However, such an approach is not applicable in boundary layers subjected to significant free-stream turbulence. An alternative methodology consists in estimating u^* from the shear-driven flow within the liquid, invoking the continuity of shear

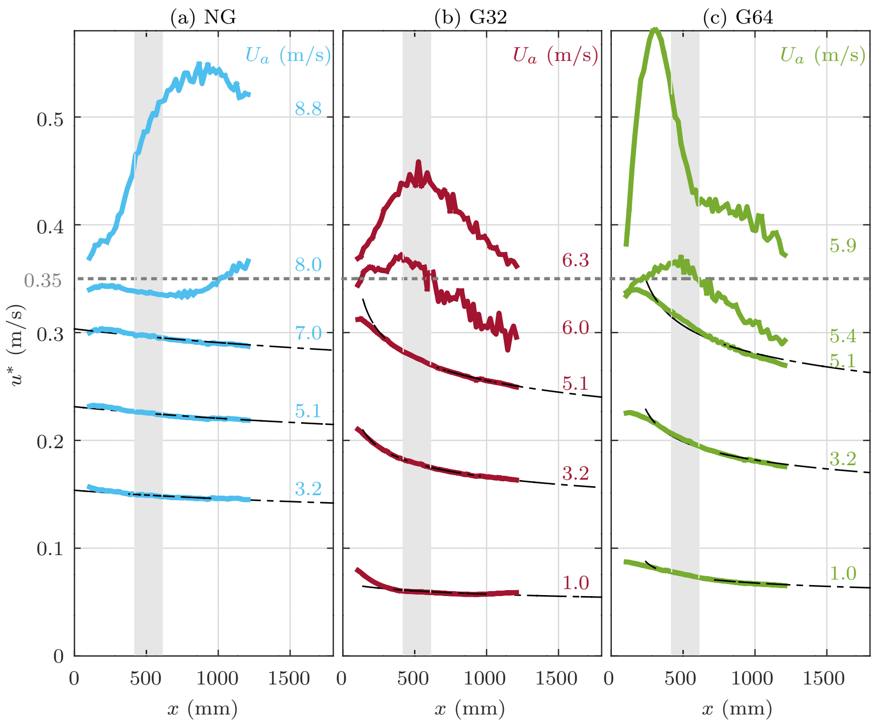

Figure 3. Streamwise evolution of u^* inferred from PIV measurements in the liquid. (a) no grid; (b) grid G32; (c) grid G64. Dashed lines are fits using the Schlichting law using Eqn. (4), with $C = 0.029$ and $x_0 = -1530\,\mathrm{mm}$ (no grid), $C = 0.032$ and $x_0 = 0\,\mathrm{mm}$ (G32) and $C = 0.038$ and $x_0 = 150\,\mathrm{mm}$ (G64). The horizontal dotted line $u^* = 0.35$ m s^{-1} corresponds to the critical friction velocity marking the wrinkle-wave transition. The light grey strip depicts the FS-SS measurement extent.

stress across the interface (Paquier *et al.*, 2015). In the present experiments, the relatively high liquid viscosity ensures that the flow induced by the wind stress remains laminar, as indicated by a maximum Reynolds number of $U_s h/\nu_\ell \approx 40$, where U_s denotes the surface drift velocity and h the liquid depth. Under the assumptions of two-dimensional flow and zero net flow rate, the velocity field adopts a parabolic Couette–Poiseuille profile (Spurk & Aksel, 2008),

$$u_\ell(x,z) = U_s(x)\left(1+\frac{z}{h}\right)\left(1+3\frac{z}{h}\right), \tag{2}$$

with $-h < z < 0$. The continuity of shear stresses at the air-liquid interface implies

$$\rho_a u^{*2} = \rho_\ell \nu_\ell \frac{\partial u_\ell}{\partial z}\Big|_{z=0}. \tag{3}$$

To determine the friction velocity u^*, we fit the velocity profile near the surface using the parabolic law (2). By differentiating this profile with respect to z and extrapolating $z \to 0$, we then obtain u^* from (3). Figure 3 presents the resulting streamwise evolution of u^* for various wind speeds U_a and for the three inlet conditions. A clear transition is observed for each inlet condition: while u^* decreases gradually with x at low wind speeds (wrinkle regime), it displays a strongly non-monotonic behaviour at higher wind speeds (wave regime).

In the absence of grid, the friction velocity follows the classical Schlichting's law (Schlichting, 2000),

$$\frac{u^{*2}}{U_a^2} = C Re_x^{-0.2}, \tag{4}$$

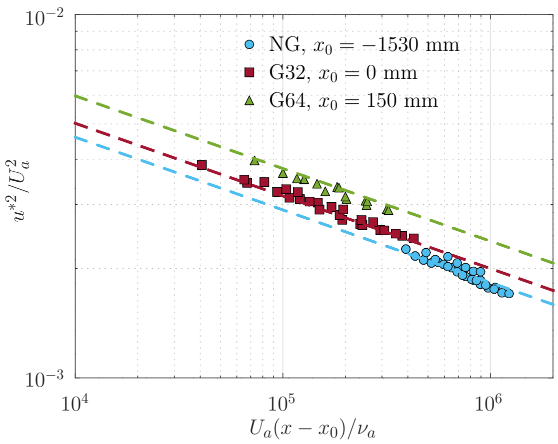

Figure 4. Evolution of the normalised friction velocity squared against the Reynolds number Re_x only for wind speeds U_a within the wrinkle regime. The dashed lines correspond to the Schlichting law of Eqn. (4), with a pre-factor $C = 0.029$ (NG), $C = 0.032$ (G32) and $C = 0.038$ (G64), respectively.

where C is a constant and $Re_x = U_a(x - x_0)/\nu_a$, with x_0 accounting for the virtual origin of the boundary layer. A best fit gives $C = 0.029$, which aligns well with the Schlichting's law, and a virtual origin at $x_0 = -1530\,\mathrm{mm}$ located far upstream from the liquid tank. This agreement with Schlichting's law confirms that the wrinkle amplitude is sufficiently small to leave the boundary layer in the air effectively unchanged.

At low wind speeds, the friction velocity increases significantly with free-stream turbulence, reaching values about 20% higher for G32 and 30% higher for G64 compared to the no-

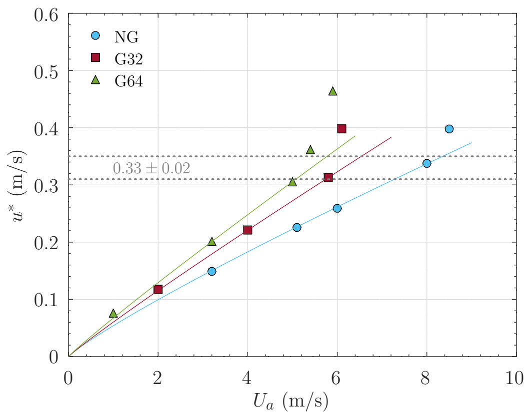

Figure 5. Evolution of u^* against U_a, at fetch $x = 500$ mm, for all inflow conditions. Solid lines are fits of the form $u^* = \alpha U_a^p$, with $p = 0.88$ (NG), and $p = 0.94$ (G32 and G64).

grid condition. However, it exhibits a steeper decrease along the streamwise direction. Despite this increase, the effect remains moderate relative to the rise in free-stream turbulence, which is amplified by a factor of 7 for the G32 and 14 for G64. The friction velocity still follows the Schlichting's law in the presence of grids, but with a larger value of C (+10% for G32 and +30% for G64), as well as a virtual origin that is noticeably shifted toward the grid location ($x_0 = 0$ mm and $x_0 = 150$ mm, for G32 and G34 respectively). This shift suggests that the boundary layer is tripped and reconfigured by the presence of the grid.

This monotonic behaviour of the friction velocity with streamwise distance holds only in the wrinkles regime, below a critical friction velocity u_c^*, which depends on both the parameters U_a and x. From figure 3, it can be seen that this transition occurs at $u^* \simeq 0.33$–0.35 m s^{-1}, a value consistent with the threshold $u_c^* \simeq 0.34$ m s^{-1} reported by Aulnette *et al.* (2022) under similar conditions. This sharp rise in u^* beyond the transition emphasises that increasing surface roughness due to waves significantly enhances the surface stress at the interface. It should be emphasised that, although the transition occurs at a relatively constant friction velocity u_c^* regardless of inlet conditions, the corresponding wind speed shows a strong dependence on these conditions. In particular, it decreases significantly with increasing free-stream turbulence: the transition occurs at about $U_{ac} = 8$ m s^{-1} in the absence of a grid, while it typically occurs around 6 m s^{-1} and 5 m s^{-1} for cases G32 and G64, respectively. This effect is clearly illustrated in figure 5, which shows the evolution of the friction velocity u^* as a function of the wind speed U_a at a given fetch.

Effect on surface deformation

Examples of instantaneous snapshots of the surface deformation measured by Free-Surface Synthetic Schlieren are given in figure 6 for different wind speeds and for each free-stream condition. There is a stark contrast between low and higher velocities. At low velocity, the interface is made up of disorganised patterns of low amplitude of about ±15 µm, that are elongated in the streamwise direction, and are typical of wrinkles. Close to the onset of the waves, two-dimensional crests oriented in the spanwise direction appeared, superimposed on the existing wrinkles, leading to an overall increase in surface amplitude up to approximately ±30 µm. At higher speeds, quasi-two-dimensional structures that span across the entire field of view with amplitudes up to ±0.4 mm are visible, which is characteristic of gravity-capillary waves. These findings qualitatively agree with the observations reported by Paquier *et al.* (2015), who conducted experiments in a wind tunnel without a grid, yielding a free-stream turbulence level of $T_u \simeq 2\%$. More importantly, figure 6 clearly illustrates the main effects of increasing the free-stream turbulence intensity: an increase in the amplitude of deformations − both in the wrinkles and waves regimes − and a significant reduction in the critical wind speed for the onset of regular waves.

The characteristic amplitude of the surface vertical displacements is defined as

$$\zeta_{\rm rms}(x) = \left\langle \overline{\zeta^2(x,y,t)} \right\rangle^{1/2}, \tag{5}$$

where the averaging is performed first in time (overbar) and then along the spanwise direction (brackets). The evolution of ζ_{rms} for a given fetch x, is depicted in figure 7 against, (a) the wind speed, and (b) the local friction velocity. The three inlet conditions follow the expected behaviour, namely a slow (linear) increase in the wrinkle regime, followed by a sharp one after the transition to the wave regime. However, the significant decrease of the critical wind speed velocity discussed above is clearly visible. From the intercept of the best fit of the two branches, wrinkles and waves, we can determine precisely the critical wind speed of the wrinkle-wave transition: $U_{ac} = 8.0 \pm 0.1$ m s^{-1} in the absence of a grid, and at $U_{ac} = 5.9 \pm 0.1$ m s^{-1}, and 5.1 ± 0.1 m s^{-1} in the G32 and G64 cases, respectively. It should be emphasised that these velocities are consistent with the change in slope observed in curves $u^*(U_a)$ (Fig. 5). The marked reduction in U_{ac} when a grid is present suggests that the extra turbulent intensity generated results in an increase of the wrinkle amplitude, which in turn allows the wrinkle-wave transition to take place at a lower wind speed.

When ζ_{rms} is plotted against the local friction velocity (Fig. 7b), data obtained under all inlet conditions collapse satisfactorily, with a transition occurring at $u_c^* \simeq 0.33 \pm 0.02$ m s^{-1}. This behaviour confirms that the abrupt increase in u^* is directly associated with the wrinkle–wave transition. Figure 7b also indicates that the transition occurs at a characteristic surface deformation of the order of $\zeta_{rms} \simeq 16 \pm 4$ µm, supporting previous findings that wrinkles act as precursors to wave development. A power-law fit of the form $\zeta_{rms} \propto u^{*n}$ within the wrinkle regime yields an exponent $n \simeq 1.1 \pm 0.1$ This value is consistent with the experimental results of Paquier *et al.* (2016), who reported exponents in the range $n \simeq 1.1$–1.2 for viscosities close to the one considered here ($\nu_\ell = 30 \times 10^{-6}$ m^{2}s^{-1} and 85×10^{-6} m^{2}s^{-1}). This near-linear dependence of ζ_{rms} therefore appears to be a robust characteristic of the wrinkle regime.

The wrinkles can be interpreted as transient wakes generated by turbulent pressure fluctuations moving within the boundary layer. Their width is mainly determined by the size of the pressure fluctuations, which scales with the boundary layer thickness, while their length depends on the wake dynamics of these moving pressure sources. Consequently, any modification of the boundary layer properties is likely to influence their geometry. To describe the shape of these surface deformations, a two-point correlation function is employed,

$$C(\mathbf{r}) = \frac{\langle \zeta(\mathbf{x},t)\zeta(\mathbf{x}+\mathbf{r},t)\rangle}{\langle \zeta(\mathbf{x},t)^2\rangle}, \tag{6}$$

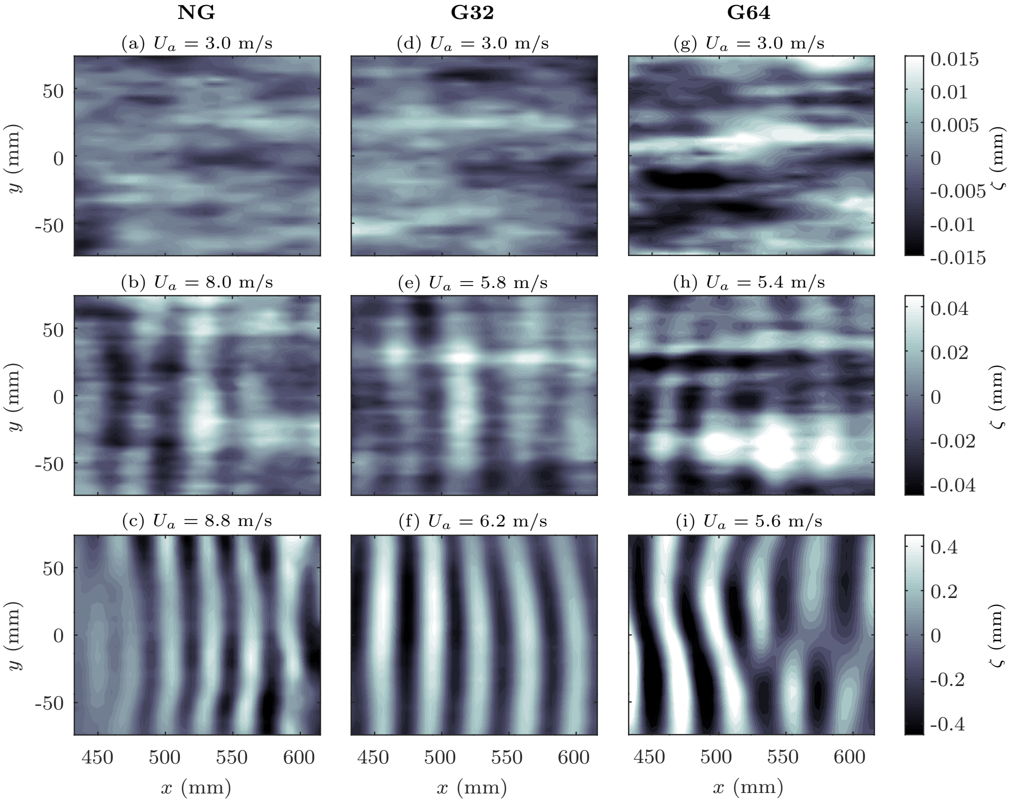

Figure 6. Examples of instantaneous surface deformation height $\zeta(x,y,t)$ without grid (a,b,c), with grid G32 (d,e,f) and with grid G64 (g,h,i), for different wind speeds U_a.

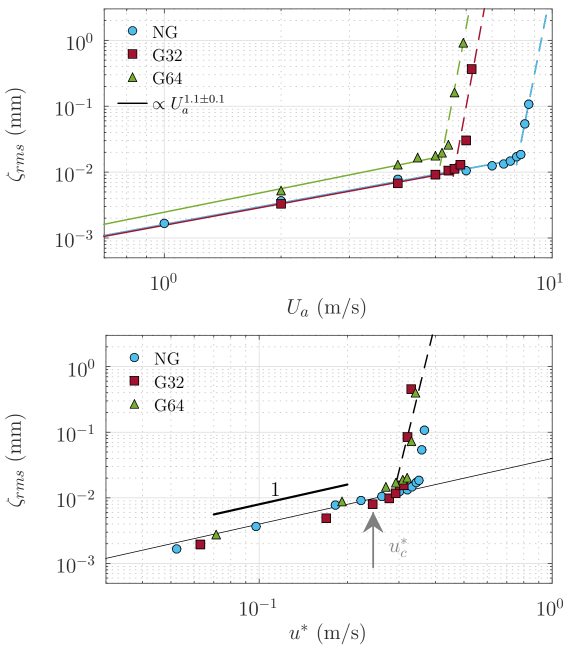

Figure 7. Evolution of $\zeta_{\rm rms}$, at $x = 500$ mm, against (a) the wind speed U_a; and (b) the local friction velocity u^*. The dashed lines in the wave regime correspond to power-law scaling shown as a guide.

where $\mathbf{r} = r_x\mathbf{e_x} + r_y\mathbf{e_y}$, and $\langle . \rangle$ indicate double average over space and time. In the case of disorganised wrinkles, the characteristic wavelengths of the deformation pattern in the longitudinal and transverse directions, Λ_i (with $i = x, y$), are then defined as $\Lambda_i = 6r_{i0}$, where r_{i0} is the position of the first zero-crossing of $C(r_i)$. Under this definition, Λ_i equals the wavelength λ of a monochromatic wave field propagating in the direction $\mathbf{e}_i$.

Figure 8 shows how the longitudinal and transverse correlation lengths vary with friction velocity for different inflow conditions. A clear crossover between Λ_x and Λ_y occurs at the critical friction velocity $u^* \simeq u_c^*$ (indicated by the grey band in the figure), marking the transition from disorganised wrinkles to nearly two-dimensional waves. Below this transition, wrinkles have a nearly constant width, while their length increases with friction velocity, consistent with wake dynamics (Rabaud & Moisy, 2013; Nové-Josserand *et al.*, 2020). Above the transition, the longitudinal length decreases to the typical wavelength of regular waves, $\Lambda_x \simeq 40$ mm, while the transverse length increases significantly (in case of purely two-dimensional waves $\Lambda_y = \infty$). Overall, inlet conditions have a limited but noticeable effect. In the wrinkle regime, grids enhance the growth of Λ_x (Fig. 8c), likely due to larger pressure structures. After the transition, differences in Λ_y suggest that inlet conditions can influence the degree of two-dimensionality of the wave field, as evidenced by a moderate increase of Λ_y for the G64 grid (Fig. 8c) consistent with figure 6(i), where the waves begin to lose their two-dimensional character.

Summary

We experimentally examined how the intensity of free-stream turbulence, T_u, in an airflow over a quiescent liquid surface affects the initial formation of wrinkles and, subsequently, waves as the wind velocity U_a increases. To this end, we employed various passive grids positioned at the inlet of the test section to generate T_u of up to 8% at the measurement location,

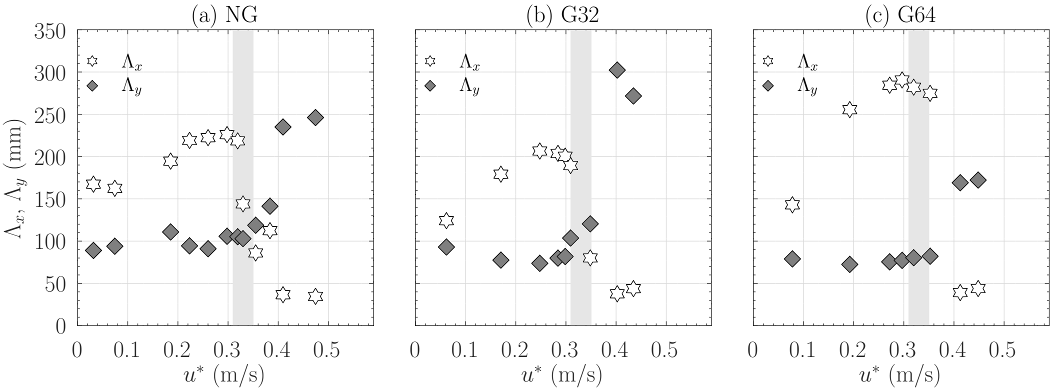

Figure 8. Streamwise evolution of the correlation lengths Λ_x and transverse Λ_y against the friction velocity u^*, averaged over the window $x \in [430, 620]$ mm, (a) NG, (b) G32, and (c) G64. The light grey strip corresponds to the critical friction velocity $u_c^* = 0.33 \pm 0.02$ m s^{-1}.

situated approximately 500 mm downstream from the start of the liquid tank. Our main findings are summarised as follows:

(a) Increasing T_u raises the friction velocity at the interface by approximately 20–30%. For all inlet conditions, the streamwise decay of u^* (below wave onset) follows Schlichting's law for a standard boundary layer over rigid surfaces, though with a modified prefactor and virtual origin when grids are used.

(b) The level of T_u does not change the typical wave-generation scenario: as wind speed rises, wrinkles form at the interface and eventually develop into regular waves at sufficiently high velocities (Paquier *et al.*, 2015, 2016), with minimal impact on their spatial organization.

(c) However, the critical wind speed U_{ac} at transition decreases markedly: $U_{ac} \simeq 8$ m s^{-1} for $T_u = 0.6\%$, 5.9 m s^{-1} for $T_u = 4\%$, and 5.1 m s^{-1} for $T_u = 8\%$. Despite this, the critical local friction velocity remains nearly constant for all inlet conditions, $u_c^* \simeq 0.33 \pm 0.02$ m s^{-1}.

(d) At the wrinkles-to-waves transition, a sharp increase is observed in both the local wave amplitude $\zeta_{rms}(x)$ and the local friction velocity $u^*(x)$.

More comprehensive details of this work are available in Mathis *et al.* (2026).

These results raise questions about the nature of the transition from wrinkles to waves and the origin of the critical friction velocity, u_c^*. Notably, this transition occurs at a constant wrinkle amplitude, ζ_{rms}. Adjusting the boundary layer properties allows us to quantify the link between turbulent forcing and the surface response, while also exploring the transition between the Phillips mechanism (Phillips, 1957) – thought to drive wrinkle formation – and the Miles mechanism (Miles, 1957), which is believed to control wave growth.

REFERENCES

Aulnette, M., Zhang, J., Rabaud, M. & Moisy, F. 2022 Kelvin-Helmholtz instability and formation of viscous solitons on highly viscous liquids. *Phys. Rev. Fluids* **7**, 014003.

Janssen, P. 2004 *The Interaction of Ocean Waves and Wind*. Cambridge University Press.

Lavoie, P., Djenidi, L. & Antonio, R. A. 2007 Effects of initial conditions in decaying turbulence generated by passive grids. *J. Fluid Mech.* **585**, 395–420.

Mathis, R., Cazin, S., Methel, J., Charru, F., Magnaudet, J., Moisy, F. & Rabaud, M. 2026 Effect of wind turbulence on wave generation over a viscous liquid. *arXiv preprint arXiv:2601.20396* .

Miles, J. W. 1957 On the generation of surface waves by shear flows. *J. Fluid Mech.* **3**, 185–204.

Mohamed, M. S. & LaRue, J. C. 1990 The decay power law in grid-generated turbulence. *J. Fluid Mech.* **219**, 195–214.

Moisy, F., Rabaud, M. & Salsac, K. 2009 A synthetic Schlieren method for the measurement of the topography of a liquid interface. *Exp. Fluids* **46**, 1021–1036.

Nové-Josserand, C., Perrard, S., Lozano-Duran, A., Benzaquen, M., Rabaud, M. & Moisy, F. 2020 Effect of a weak current on wind-generated waves in the wrinkle regime. *Phys. Rev. Fluids* **5**, 124801.

Paquier, A., Moisy, F. & Rabaud, M. 2015 Surface deformations and wave generation by wind blowing over a viscous liquid. *Phys. Fluids* **27**, 122103.

Paquier, A., Moisy, F. & Rabaud, M. 2016 Viscosity effects in wind wave generation. *Phys. Rev. Fluids* **1**, 083901.

Perrard, S., Lozano-Durán, A., Rabaud, M., Benzaquen, M. & Moisy, F. 2019 Turbulent windprint on a liquid surface. *J. Fluid Mech.* **873**, 1020–1054.

Phillips, O. M. 1957 On the generation of waves by turbulent wind. *J. Fluid Mech.* **2**, 417–445.

Rabaud, Marc & Moisy, Frédéric 2013 Ship wakes: Kelvin or Mach angle? *Phys. Rev. Lett.* **110** (21), 214503.

Roach, PE 1987 The generation of nearly isotropic turbulence by means of grids. *International journal of heat and fluid flow* **8** (2), 82–92.

Schlichting, H. 2000 *Boundary Layer Theory*, 8th edn. Springer.

Spurk, J. H. & Aksel, N. 2008 *Fluid Mechanics*, 2nd edn. Springer.

Sullivan, P. P. & McWilliams, J. C. 2010 Dynamics of winds and currents coupled to surface waves. *Annu. Rev. Fluid Mech* **42**, 19–42.

Zhao, Y., Yang, Y., Li, M & Peng, Y. 2023 Measurements of decaying grid turbulence with various initial conditions. *Eur. J. Mech. B-Fluids* **102**, 46–55.